

# Dynamical damping terms for symmetry-seeking shift conditions

Daniela Alic,<sup>1</sup> Luciano Rezzolla,<sup>1,2</sup> Ian Hinder,<sup>1</sup> and Philipp Mösta<sup>1</sup>

<sup>1</sup> *Max-Planck-Institut für Gravitationsphysik, Albert-Einstein-Institut, Potsdam-Golm, Germany*

<sup>2</sup> *Department of Physics and Astronomy, Louisiana State University, Baton Rouge, LA, USA*

(Dated: October 31, 2018)

Suitable gauge conditions are fundamental for stable and accurate numerical-relativity simulations of inspiralling compact binaries. A number of well-studied conditions have been developed over the last decade for both the lapse and the shift and these have been successfully used both in vacuum and non-vacuum spacetimes when simulating binaries with comparable masses. At the same time, recent evidence has emerged that the standard “Gamma-driver” shift condition requires a careful and non-trivial tuning of its parameters to ensure long-term stable evolutions of unequal-mass binaries. We present a novel gauge condition in which the damping constant is promoted to be a dynamical variable and the solution of an evolution equation. We show that this choice removes the need for special tuning and provides a shift damping term which is free of instabilities in our simulations and dynamically adapts to the individual positions and masses of the binary black-hole system. Our gauge condition also reduces the variations in the coordinate size of the apparent horizon of the larger black hole and could therefore be useful when simulating binaries with very small mass ratios.

PACS numbers: 04.40.-b, 04.40.Dg, 95.35.+d

## I. INTRODUCTION

Five years after the first demonstrations [1–3] that the numerical solution of the inspiral and merger of binary black holes (BBHs) was within the technical and computational capabilities of many numerical-relativity groups, our understanding of this process has expanded beyond the most optimistic predictions. Numerical-relativity simulations of black-hole binaries have been performed in a large region of the possible space of parameters (see [4, 5] for two recent reviews). In addition, the results of these simulations have been exploited on several fronts. In gravitational wave data analysis, they have been used to produce template banks that increase the distance reach of detectors [6–8] and to aid the calibration of search pipelines [9–11]. In astrophysics they have been used to determine the properties of the final black hole (BH) of a BBH inspiral and merger (see [12–14] and references therein for some recent work) and hence assess the role that the merger of supermassive BHs plays in the formation of galactic structures [15, 16]. In cosmology they have been used to study the electromagnetic counterparts to the merger of supermassive BH binaries and hence deduce their redshift [17–20].

Despite this extensive and rapid progress, there are portions of the space of the parameters that still pose challenges for numerical simulations, in particular those involving binaries with BHs that are maximally spinning (but see [21] for some progress in this direction) or with small mass ratios  $q \equiv M_2/M_1 \leq 1$ . This latter problem is potentially a rather serious one since the computational costs scale in general quadratically with the inverse of the mass ratio of the system. The inspiral timescale is inversely proportional to  $q$  (the smaller BH spends more orbits per frequency interval during its inspiral onto the larger BH) and the timestep limit in explicit numerical schemes also decreases linearly with the BH size and hence inversely proportionally with  $q$ .

While some progress has been made recently when simulating binaries with mass ratios as small as  $q = 1/10$  [22, 23],

it is clear that some significant technical changes are needed in order to tackle mass-ratios which are much smaller. One of these changes may consist in adopting implicit numerical schemes in which the timestep limitation is set uniquely by the truncation error and not by the smallest spacing of the spatial numerical grid. Another improvement could come from the use of better spatial gauge conditions that, by better adapting the coordinates to the different curvatures of the spatial slice, may reduce the numerical error and hence the computational cost. Recent numerical simulations have revealed that the standard “Gamma-driver” shift condition [24] requires a careful tuning of its parameters to ensure long-term stable BBH evolutions when considering unequal-mass binaries. Work to alleviate some of these problems has been recently started [25–27] and has so far concentrated on adapting the damping term  $\eta$  in the shift condition (see Sect. II for a detailed discussion of the gauge and of the damping term) to better suit the uneven distribution of local curvature on the spatial hypersurface as the binary evolves. In practice, while a constant value of  $\eta$  has worked well for comparable-mass binaries, the investigations reported in [25–27] have suggested the use of damping factors that have a spatial dependence adapted to the location of the BHs. The first non-constant prescription for  $\eta$  [25] used an expression which adapts to the mass of each BH via the conformal factor, but it was found to lead to large errors at mesh refinement boundaries [26] and so was replaced by a simpler analytical form containing constant parameters which need to be tuned to the masses of the BHs. At present it is not clear whether the tuning made with mass ratios  $q \gtrsim 0.25$  will be effective also for much smaller mass ratios.

In this paper we propose a different approach to the problem of a dynamical damping term for symmetry seeking shift conditions and promote  $\eta$  to be a fully dynamical variable, as has proven very effective for the shift vector and for the  $\tilde{\Gamma}$  variables. The resulting gauge condition dynamically adapts to the individual positions and masses of the BBH system without the need for special tuning and remains well-behaved

(*i.e.*, smooth and bounded) at all times. Considering three different options for the source term in the evolution equation for  $\eta$ , we show that an expression which is very simple to implement leads to numerical errors which are comparable to or smaller than the constant  $\eta$  case. Furthermore, this choice reduces the dynamics in the coordinate size of the apparent horizon of the smaller BH and could therefore be useful when simulating binaries with very small mass ratios.

The structure of the paper is as follows. In Sect. II we summarise the numerical infrastructure and the mathematical setup used in our simulations, while Sect. III is dedicated to a review of the slicing and spatial gauge conditions and to the discussion of our novel approach. Sections IV and V are dedicated to the discussion of the results of applying the new gauge to simulations of single nonspinning BHs (Sect. IV) and to systems with BHs having either equal or unequal masses (Sect. V). Finally, the conclusions and the prospects for future work are detailed in Sect. VI. We use a spacelike signature  $(-, +, +, +)$  and a system of units in which  $c = G = M_{\odot} = 1$ .

## II. NUMERICAL SETUP

The numerical setup used in the simulations presented here is the same one discussed in [28] and more recently applied to the `Llama` code described in [29]. The latter makes use of higher-order finite-difference algorithms (up to 8th order in space) and a multi-block structure for the outer computational domain, which allows one to move the outer boundary to a radius where it is causally disconnected from the binary. We refer the reader to the papers above for details and here simply note that we solve the Einstein equations in vacuum with a conformal and traceless formulation of the equations, in which the conformal factor has been redefined as  $W \equiv [(\det(\gamma_{ab}))^{-1/6}]$ , or in terms of the metric  $\tilde{\gamma}_{ab} = W^2\gamma_{ab}$ . The corresponding evolution equation is therefore

$$\partial_t W - \beta^i \partial_i W = \frac{1}{3} W \alpha K - \frac{1}{3} W \partial_i \beta^i, \quad (1)$$

where  $K$  is the trace of the extrinsic curvature (see [28] and [29] for details on our specific implementation).

The computational infrastructure of the `Llama` code is based on the `Cactus` framework [30, 31] and the `Carpet` [32, 33] mesh-refinement driver, and implements a system of multiple grid patches with data exchanged via interpolation [29]. We use a central cubical Cartesian patch containing multiple levels of adaptive mesh refinement, with higher resolution boxes tracking the location of each BH, *i.e.*, “moving boxes”. This is surrounded by 6 additional patches with the grid points arranged in a spherical-type geometry, with constant angular resolution to best match the resolution requirements of radially outgoing waves. This allows us to evolve out to very large radii at a tiny fraction of the computational cost which would be necessary to achieve the same resolution with a purely Cartesian code. We use one patch for each of the  $\pm x$ ,  $\pm y$  and  $\pm z$  axes, which leads to an inner spherical inter-patch boundary and to a spherical outer boundary. The latter

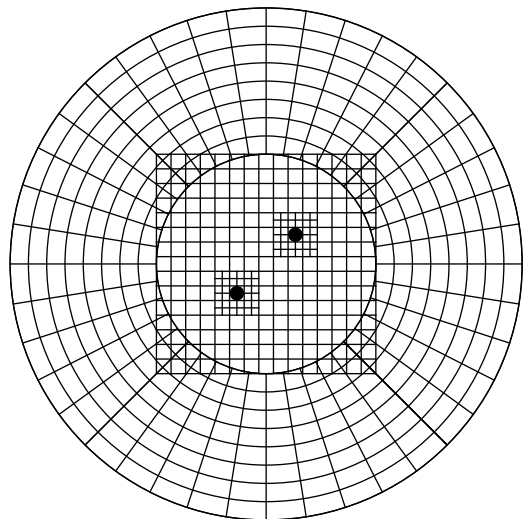


FIG. 1: Schematic diagram of a typical `Llama` grid setup in the  $(x, y)$  plane. Note the inner Cartesian grid with box-in-box AMR which is joined to a 6-patch multiblock structure (only 4 of these patches are shown in the  $(x, y)$  plane).

can be placed at very large distances and we choose it to be it causally disconnected from the surfaces on which we compute the waveforms for the duration of the simulation. Figure 1 shows a schematic diagram of a typical `Llama` grid setup in the  $(x, y)$  plane. Note the inner Cartesian grid with moving-boxes which is joined to a 6-patch multiblock structure (only 4 of these patches are shown in the  $(x, y)$  plane). The detailed grid structure used in each run is listed in Table I, and for the purpose of comparison, the resolution of each simulation is indicated by the grid spacing  $h_0/M$  of the coarsest Cartesian grid. The unit  $M$  is chosen such that each BH has mass  $0.5M$  in both the single and binary BH cases. In all cases the coarsest resolution is also equal to the radial spacing in the angular patches.

## III. GAUGE CONDITIONS AND DYNAMICAL DAMPING TERM

As mentioned in the introduction, for the formulation of the Einstein equations we adopt, the use of suitable gauge conditions was the last obstacle to overcome in order to obtain long-term stable simulations of BBHs [2, 3]. In what is now the standard *moving-puncture* recipe, the lapse  $\alpha$  is evolved using a singularity-avoiding slicing condition from the  $1 + \log$  family [34]

$$\partial_t \alpha - \beta^i \partial_i \alpha = -2\alpha K, \quad (2)$$

while the shift vector  $\beta^i$  is evolved using the hyperbolic Gamma-driver condition [24]

$$\partial_t \beta^a - \beta^i \partial_i \beta^a = \frac{3}{4} B^a, \quad (3)$$

$$\partial_t B^a - \beta^i \partial_i B^a = \partial_t \tilde{\Gamma}^a - \beta^i \partial_i \tilde{\Gamma}^a - \eta B^a. \quad (4)$$

Configuration	$h_0/M$	$N_{\text{ang.}}$	$R_{\text{in}}/M$	$R_{\text{out}}/M$	$N_{\text{lev.}}$	$r_1/M$
single BH	0.96	21	39.36	400.00	6	(12, 6, 3, 1.5, 0.6)
BBH, $q = 1$	0.96	21	39.36	1980.48	6	(12, 6, 3, 1.5, 0.6)
BBH, $q = 1/4$	(0.8, 0.96, 1.12)	(23, 27, 33)	49.92	2545.92	(6, 8)	(12, 6, 3, 1.5, 0.8, 0.4, 0.2)

TABLE I: Numerical grid parameters of each BH configuration studied.  $h_0$  is the grid spacing on the coarsest Cartesian grid, which is equal in all cases to the radial grid spacing in the angular patches.  $N_{\text{ang.}}$  is the number of cells in the angular directions in the angular patches.  $R_{\text{in}}$  and  $R_{\text{out}}$  are the inner and outer radii of the angular patches.  $N_{\text{lev.}}$  is the number of refinement levels (including the coarsest) on the Cartesian grid, and  $r_1$  indicates that a cubical refinement box of side  $2r_1$  is centred on the BH on level “1”, with level 0 being the coarsest (in the case that the boxes overlap, they are replaced with a single box enclosing the two). The unit  $M$  is chosen such that each BH has mass  $0.5M$  in both the single and binary BH cases.

We recall that the Gamma-driver shift condition is similar to the Gamma-freezing condition  $\partial_t \tilde{\Gamma}^k = 0$  which, in turn, is closely related to the minimal distortion shift condition [35]. The differences between these two conditions involve the Christoffel symbols and are basically due to the fact that the minimal distortion condition is covariant, while the Gamma-freezing condition is not (see the discussion in [36]).

The coefficient  $\eta$  of the last term in (4) is usually referred to as the damping term and plays a fundamental role in our investigation. It was originally introduced to avoid strong oscillations in the shift and experience has shown that by tuning its value, it is possible to essentially “freeze” the evolution of the system at late times [37]. In simulations of inspiralling compact binaries this damping term is typically set to be constant in space and time and equal to  $2/M$  for BBHs and equal to  $1/M$  for binaries of neutron stars, where  $M$  is the sum of the masses of the BHs or neutron stars [38, 39]. Similar values have also been shown to yield stable evolutions in the case of mixed binaries with mass ratios  $q \simeq 1/6$  [40]. While this choice works well for binaries with comparable masses, a simple dimensional argument shows that it will cease to be a good one for binaries with unequal masses. Since the dimension of  $\eta$  is inverse mass, and the relevant mass is the mass of each individual BH, as the BH mass decreases a larger value of  $\eta$  will be needed to maintain a similar damping effect. For an unequal mass system, this is impossible with a constant  $\eta$ .

### 1. Position-Dependent Damping Term

To overcome the limitations imposed by a constant-in-space damping term, various recipes have been proposed recently in the literature. A first suggestion was presented in Ref. [25], where the damping term was specified by the function

$$\eta_{\text{MB}}(r) = R_0 \frac{\sqrt{\tilde{\gamma}^{ij} \partial_i W \partial_j W}}{(1 - W)^2}, \quad (5)$$

where  $\tilde{\gamma}^{ij}$  is the inverse of the conformal 3-metric and  $R_0$  is a dimensionless constant chosen in such a way that  $R_0 M_{\text{BH}}$  corresponds to the Schwarzschild radial coordinate for the stationary state, *i.e.*,  $R_0 \simeq 1.31241$  [41]. However, as discussed subsequently by the same authors [26], expression (5) leads to sharp features (spikes) which can produce coordinate drifts

and affect the stability of the simulations. To remove these drawbacks, alternative forms were suggested that read respectively [26]

$$\eta_{\text{MGB}} = A + \frac{C_1}{1 + w_1 (\hat{r}_1^2)^n} + \frac{C_2}{1 + w_2 (\hat{r}_2^2)^n}, \quad (6)$$

and

$$\eta_{\text{MGB}} = A + C_1 e^{-w_1 (\hat{r}_1^2)^n} + C_2 e^{-w_2 (\hat{r}_2^2)^n}, \quad (7)$$

where  $w_1$  and  $w_2$  are positive parameters chosen to change the width of the functions based on the masses of the two BHs. The power  $n$  is a positive integer which determines the fall-off rate, while the constants  $A$ ,  $C_1$ , and  $C_2$  are chosen to provide the desired values of  $\eta$  at the punctures and at infinity. Finally, the dimensionless radii  $\hat{r}_1$  and  $\hat{r}_2$  are defined as  $\hat{r}_i = |\vec{r}_i - \vec{r}| / |\vec{r}_1 - \vec{r}_2|$ , where  $i$  is either 1 or 2, and  $\vec{r}_i$  is the position of the  $i$ -th BH. In addition to the new prescriptions (6)–(7), which provide appropriate values both near the individual punctures and far away from them with a smooth transition in between, there is evidence that they also lead to a smaller truncation error. In particular, when examined for  $w_1 = w_2 = 12$ ,  $n = 1$ , the waveforms produced when using Eq. (6) showed less deviation with increasing resolution than using a constant  $\eta$ . Similar results were found when using Eq. (7), leading the authors to the conclusion that the preferred definition for the damping term is Eq. (6) because it is computationally less expensive.

It was shown recently [27] for the Gamma-driver shift condition that there is a stability limit on the time step size which depends on  $\eta$ . This limitation comes from the time integrator only and is not dependent on spatial resolution. One of the proposed solutions to this problem is to taper  $\eta$  with a functional dependence of the type

$$\eta_{\text{S}}(r) = \eta_0 \frac{R^2}{r^2 + R^2}, \quad (8)$$

where  $r$  is the coordinate distance from the centre of the BH and  $R$  is the radius at which one makes the transition between an inner region where  $\eta_{\text{S}}$  is approximately equal to  $\eta_0$  and an outer region where  $\eta_{\text{S}}$  gradually decreases to zero. We find that this form does indeed help in removing potential instabilities and, as we will discuss in the following section, can be used also for a fully dynamical definition for the damping term.

## 2. Evolved Damping Term

While the analytic prescriptions discussed in the previous section have been shown to be effective when suitably tuned, it is not clear whether they will be equally effective for different mass ratios, nor how to choose the parameters without case-by-case tuning. In view of this and in order to derive an expression which adapts dynamically in space and time to the local variations of the shift vector, we have promoted the damping term to be an evolved variable with the simple equation

$$\partial_t \eta - \beta^i \partial_i \eta = \frac{1}{M} (-\eta + S(r)). \quad (9)$$

The function  $S(r)$  is a position-dependent source term which can be chosen freely. The first term on the right-hand-side is introduced to induce an exponential decay of the damping term towards  $S(r)$  such that in the steady state,  $\eta \rightarrow S(r)$ . The advective derivative term  $\beta^i \partial_i \eta$  ensures that the motion of the punctures, which are locally advected by  $\beta^i$ , is taken into account in the driving of  $\eta \rightarrow S(r)$  (we want to drive  $\eta$  to a specific behaviour in the neighbourhood of the punctures). To better interpret our suggestion for the dynamical gauge (9), it is useful to compare it with a simpler ordinary differential equation

$$\tau \frac{d\eta}{dt} = -\eta + S(t). \quad (10)$$

Setting now  $\eta_0 \equiv \eta(t=0)$ ,  $S_0 \equiv S(t=0)$ , and assuming that  $\tau(dS/dt) \ll 1$  so that it can be neglected at first order, Eq. (10) would have solution

$$\eta \simeq S + (\eta_0 - S_0)e^{-t/\tau}, \quad (11)$$

and thus  $\eta \rightarrow S$  as  $t \rightarrow \infty$ . Although in the case of our gauge-evolution equation (9), the source term is time-dependent and sometimes the time derivative can be rather large, especially near the punctures, equation (10) is useful to recognise that the damping term is itself damped and driven to the solution given by the source function  $S$ .

The arbitrariness in the form of  $S(r)$  is removed in part by the works discussed in the previous sections and hence a first possible form is inspired by (5) and thus given by

$$S_1(r) = \eta_{\text{MB}}(r) = R_0 \frac{\sqrt{\tilde{\gamma}^{ij} \partial_i W \partial_j W}}{(1-W)^2}. \quad (12)$$

As we will discuss in the next sections, this choice works very well for single BHs, leading to smoother profiles for  $\eta$  and consequently more stable evolutions. Similarly, another convenient choice for the source is a combination of expression (5) and (8)

$$S_2(r) = \eta_{\text{MB}}(r) \eta_{\text{S}}(r) = \left( R_0 \frac{\sqrt{\tilde{\gamma}^{ij} \partial_i W \partial_j W}}{(1-W)^2} \right) \left( \frac{R^2}{r^2 + R^2} \right), \quad (13)$$

This choice ensures that  $\eta$  is dynamically adapting in the inner region due to the  $\eta_{\text{MB}}$  factor, while in the outer region the

$\eta_{\text{S}}$  factor ensures minimal dynamics and implements the suggestion of Ref. [27] that  $\eta \rightarrow 0$  at large radius to avoid the instability there.

The generalisation of the source term (13) to the case of a binary system is straightforwardly given by

$$S_3(r) = \left( R_0 \frac{\sqrt{\tilde{\gamma}^{ij} \partial_i W \partial_j W}}{(1-W)^2} \right) \left( \frac{R^2}{r_1^2 + r_2^2 + R^2} \right), \quad (14)$$

where  $\vec{r}_1, \vec{r}_2$  are the distances from  $\vec{r}$  to the individual BHs centres.

The following sections will be dedicated to the results of simulations performed with the evolution equation for the damping term (9) to study nonspinning single BHs via the source terms (12)–(13), and to evolve BBHs via the source term (14). As a final remark we note that although our dynamical gauge requires the numerical solution of an additional equation [*i.e.*, Eq. (9)], the associated computational costs are minimal, given that we are evolving a scalar quantity and that the evolution equation is very similar to those already implemented within the Gamma-driver condition. More specifically, the added computational costs range from 1 to 2% depending on the complexity and length of the simulation (the longer the simulation, the larger the impact of frequent restarts and thus the smaller the impact of the additional evolution equation).

## IV. APPLICATION OF THE NEW GAUGE: SINGLE BLACK HOLES

We next examine the properties of the new dynamical gauge (9) for the damping factor and present its advantages when compared with the other position- and mass-dependent suggestions presented in the previous section. Specifically, we will study the  $\eta_{\text{MB}}(r)$  and  $\eta_{\text{S}}(r)$  prescribed forms for  $\eta$ , and compare them with both the  $S_1(r)$  and  $S_3(r)$  variants of the evolved gauge condition (9). We will start by considering the simple case of a single nonspinning puncture.

Fig. 2 shows a comparison between an evolution using the prescription  $\eta_{\text{MB}}(r)$  provided by Eq. (5) (red dashed lines) and the new gauge using as source  $S_1(r)$  from Eq. (12) (blue solid lines). In both cases, the value of the damping factor at the puncture adapts automatically to the mass of the BH, due to its dependence on the conformal factor. However, when the damping term is given the form  $\eta_{\text{MB}}(r)$ , large spikes develop at the origin at late times and noise travels outwards as the gauge settles (*cf.* left panel of Fig. 2). These large noise pulses leave sharp features in  $\eta$  which might lead to coordinate drifts and eventually affect the stability when simulating BBHs. On the other hand, when evolving the damping factor and using  $\eta_{\text{MB}}(r)$  as a source, it is possible to avoid any forcing of the damping term, which is instead always the solution of the dynamical driver. This, in turn, reduces the noise and ensures long-term stability of the simulation as shown by the right panel of Fig. 2.

We can further improve the stability properties of the damping factor in the outer wave region by matching it with a

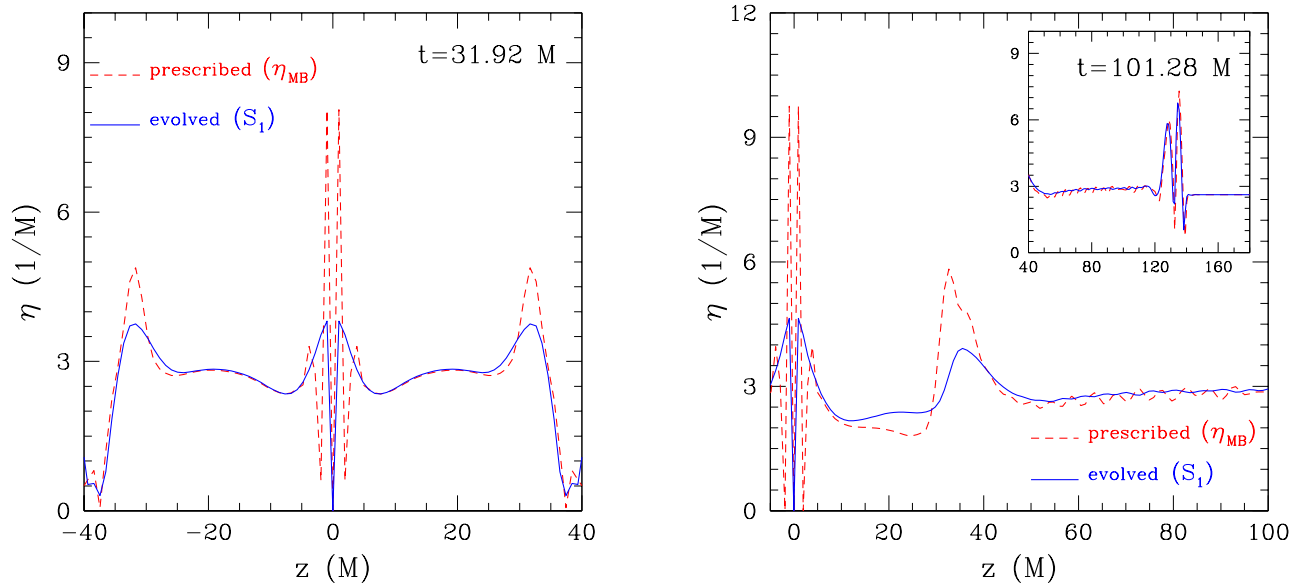


FIG. 2: Profiles along the  $z$ -axis of the damping term  $\eta$  for an isolated Schwarzschild BH. Different lines refer to the case when  $\eta$  is prescribed using Eq. (5) (red dashed line) or when evolved in time using Eq. (9) with source given by (12) (blue solid line). The left panel refers to an earlier time and focuses on the central region of the grid. The right panel refers to a later time and shows a larger portion of the grid, highlighting that in contrast to the dynamical  $\eta$ , the evolved one leads to smooth profiles at the patch boundary (see inset). Note that the outer boundary is at  $400 M$  and cannot be responsible for the appearance of the spikes via reflection.

function which drives it smoothly to zero. Fig. 3 shows a comparison between a BH evolution using the prescription  $\eta_{\text{MB}}(r)\eta_S(r)$  given by Eqs. (5) and (8) (red dashed lines), and the evolved  $\eta$  using as source Eq. (13) (blue solid lines). Note that in the case of the prescribed  $\eta_{\text{MB}}(r)\eta_S(r)$ , the outgoing gauge pulses still produces sharp features near the BH at  $z \sim 3 M$ , which are neither propagated away nor damped in-place. Moreover, sharp features far from the BH continue to be produced as the initial spikes pass through the interpatch boundaries.

Smoother profiles can instead be obtained by evolving the damping factor, using  $\eta_{\text{MB}}(r)\eta_S(r)$  as a source. This is especially true near the BH, while large variations but of small amplitude are still produced as the gauge pulses pass through the interpatch boundaries. Finally we note that in contrast to all the other evolution variables in our code, no artificial dissipation is imposed on the damping term so that the features of its evolution equation can be better appreciated.

## V. APPLICATION OF THE NEW GAUGE: BLACK-HOLE BINARIES

As shown in the previous section, our evolved damping factor leads to smoother profiles and consequently to stable BH evolutions, free of coordinate drifts. In this subsection, we study the effect of using different functional forms for the sources in the evolution equation (9).

### A. Equal-mass binaries

We first consider the evolution of an equal-mass nonspinning BH binary, whose properties can be found in Table II. For simplicity we have considered a system with small separation  $D = 7 M$ , so that overall the binary performs only about 3 orbits before merging and settles to an isolated spinning BH after about  $200 M$ .

Fig. 4 shows a comparison of the profile of the damping term on the  $z$ -axis when using the evolution equation (9) and the source term given either by  $S_1$  [cf. Eq. (12); red dashed line], or by  $S_3$  [cf. Eq. (14); blue solid line]; in both cases we have set  $R = 20 M$ .

It is clear that when using either expression for the source function, the value of  $\eta$  at the location of the punctures adapts in time through the coupling with the conformal factor  $W$ , which tracks the position and the masses of the two BHs. It is also worth noting that near the two punctures, the two evolution equations yield very similar solutions for the damping factor as one would expect since  $R_0 \gg D$ . However, when using the source (12) (red dashed line), the evolution of the damping term produces large gauge pulses which travel outwards and are amplified by the mesh-refinement and the interpatch boundaries. This is particularly evident in the right panel of Fig. 4 which refers to a later time when the BHs have already merged. These undesirable features are very effectively removed by adopting the source term (13) (blue solid line), which provides a natural fall-off for the damping term as this propagates towards the outer boundary.

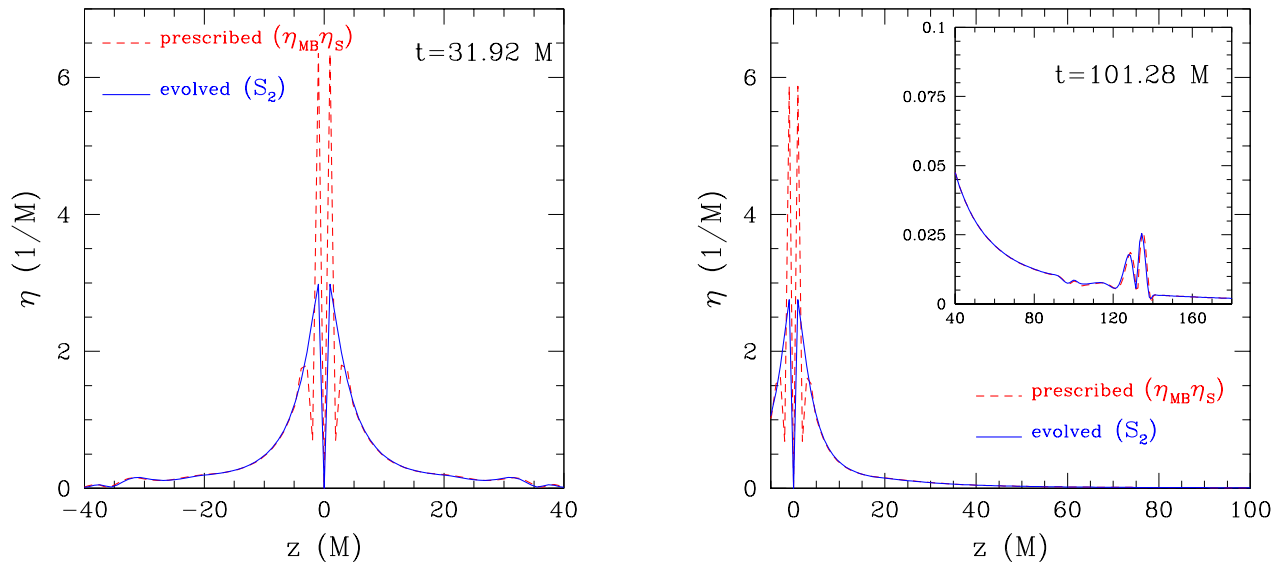


FIG. 3: The same as in Fig. 2, but the prescribed damping term Eq. (5) is tapered with a function Eq. (8), while the source term for the evolution equation is given by (13). Note that in this case the damping term falls off as expected but that in the case of the prescribed  $\eta_{\text{MB}}(r)\eta_{\text{S}}(r)$ , the outgoing gauge pulses still produces sharp features near the BH at  $z \sim 3 M$ , which do not propagate away. Moreover, sharp features are produced as the initial spikes pass through the interpatch boundaries located at  $z \sim 40 M$ . Smoother profiles can instead be obtained by evolving the damping factor.

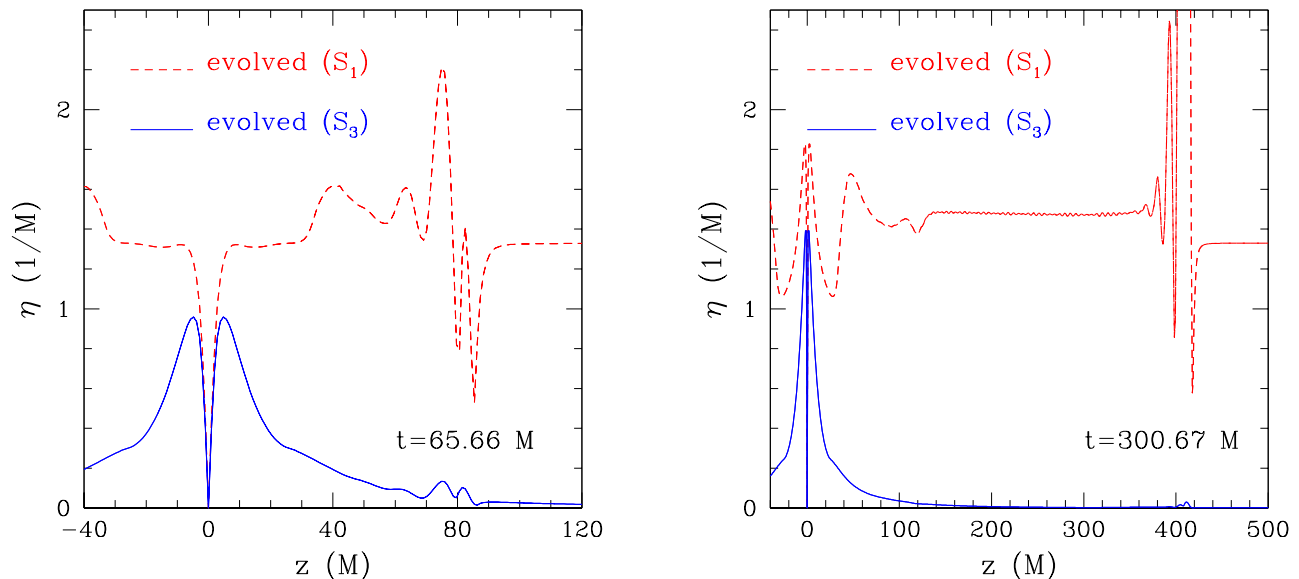


FIG. 4: Profiles along the  $z$ -axis of the damping term  $\eta$  for an *equal-mass* BBH system. Different lines refer to the case when  $\eta$  evolved with sources given respectively by (12) (red dashed line) or by (13) (blue solid line). The left and right panel refers to two different times and highlight the importance of the fall-off term to avoid reflections at mesh boundaries. Note that the outer boundary is at  $\simeq 2000 M$  and cannot be responsible for the appearance of the spikes via reflection.

### B. Unequal-mass binaries

We next consider the evolution of an unequal-mass non-spinning BH binary with mass ratio  $q = 1/4$ , initial separation  $D = 8 M$  and which performs about 4 orbits before merging

and settling to an isolated spinning BH after about  $600 M$ . A complete list of the binary's properties can be found in Table II. We find that an evolution equation for  $\eta$  is a very convenient choice also for unequal mass binary simulations.

Configuration	$m_1/M$	$m_2/M$	$x_1/M$	$x_2/M$	$P_1^x/M$	$P_1^y/M$
single BH	0.5	--	0.0	--	0.00000000	0.00000000
BBH, $q = 1$	0.5	0.5	3.5	-3.5	-0.00335831	0.12369380
BBH, $q = 1/4$	0.8	0.2	1.6	-6.4	-0.00104474	0.07293950

TABLE II: Initial data parameters for the configurations studied. Expressed in units of the total mass  $M$  are: the initial irreducible masses of the BHs (obtained by iterating over bare mass parameters)  $m_i$ , the coordinates of the BHs on the  $x$ -axis  $x_i$ , the momentum of BH 1  $P_1^i$  (the momentum of BH 2 is equal and opposite,  $P_2^i = -P_1^i$ ). The unit  $M$  is chosen such that each BH has mass  $0.5M$  in both the single and binary BH cases.

### 1. Spatial Dependence

Fig. 5 shows the spatial dependence of the damping term at some representative times. The two top panels refer to when the punctures are close to the  $x$ -axis for the cases where  $\eta$  is kept constant in space and time (red dashed line) and where it is evolved in time with a source given by (14) (blue solid line). Clearly, also in the unequal-mass case the new gauge drives the damping term to follow the BHs and to be smooth elsewhere. The bottom left and right panels show the damping term on the  $(x, y)$  plane at two times which are similar to those shown in the top panels and show the non-trivial but smooth distribution of the damping term which adapts to the motion of the punctures (the latter are near the maxima of the  $\eta$ ). The value of  $\eta$  is  $\sim 1.5/M$  near the large BH and  $\sim 4.5/M$  near the small BH, leading to a value for  $m_i \eta \sim 1$  for both BHs, where  $m_1 = 0.8M$  and  $m_2 = 0.2M$  are the irreducible masses of each BH. This demonstrates that the gauge condition is adapting the value of  $\eta$  to the mass of the BH. As an aside, we note that there is a region between the BHs where  $\eta$  drops nearly to 0, and a “wake” of low  $\eta$  which follows behind the motion of the smaller BH.

### 2. Waveforms and Errors

One of the most useful quantities calculated from a BBH simulation is the gravitational waveform. The physical waveform is that measured at future null infinity, and is independent of the gauge condition used for the evolution. In practice, waveforms are often computed at finite radii and extrapolated to future null infinity, and the gauge condition can have an effect on the extrapolation error. More importantly, different gauges can lead to different truncation errors in the evolution of the BH motion depending on how well we can reproduce a given field variable at the chosen resolution, and these errors will be reflected in the waveform errors. As a result, different gauges can in practice lead to small differences also in the calculation of the waveforms, and it is important to study the impact of the different gauges on the waveforms and their truncation errors.

In Fig. 6 we show the real part of the  $\ell = 2, m = 2$  mode of the gravitational waveform  $\Psi_4$  as extracted at  $r = 100M$ . Different lines (dotted, dashed, solid) refer to the different resolutions reported in Table I, while the two panels refer to the cases where  $\eta$  is kept constant in space and time (upper panel) and where it is evolved with a source given by  $S_3$  [cf. Eq. (14)]

(lower panel). As expected, the differences in the waveforms due to the different truncation errors for the two gauges are very small and confirm that a different prescription for the gauges does not influence the gravitational-radiation signal. Figure 7 offers a different view of the gravitational-wave signal by showing the phase difference in the  $\ell = 2, m = 2$  mode,  $\Delta\phi_{22}$ , of the waveforms as computed between the low and medium resolutions (red dashed line) and between the medium and high resolutions (blue solid line). The latter has been scaled to compensate for an 8th-order convergence which is indeed obtained as shown by the very good overlap between the dashed and solid curves during all of the inspiral, being slightly worse during the merger, when the convergence order drops. The left panel refers to the case when  $\eta$  is kept constant in space and time, while the right one refers to when it is evolved with a source given by (14) and  $R = 20M$ . Once again the phase errors are comparable between the two gauge conditions.

We see that adopting an evolution equation for the damping term allows one to reproduce with a comparable accuracy the numerical results obtained with the more standard prescription of a constant value for  $\eta$ . At the same time, however, it also shows that in this way no special tuning is required and the prescription that works well for equal-mass binaries is also very effective for an unequal-mass case with  $q = 1/4$ . We expect this to be true also for much smaller mass ratios, whose investigation goes beyond the scope of this paper but will be pursued in our future work.

### 3. Impact on the Apparent-Horizon Size

Some final consideration will now be given to the effect that the new gauge condition has on the apparent horizon (AH) coordinate size as it varies during the simulation. We recall that numerical simulations of moving punctures have routinely reported a certain dynamics in the coordinate size of the AH. This dynamics takes place during the early stages of the evolution, as the gauges evolve rapidly from their initial conditions and reach the values they are brought to by the time-dependent drivers. Although these changes are of purely gauge nature and do not influence the subsequent evolution of gauge-invariant quantities, they represent nevertheless a computational nuisance as they require a high-resolution mesh-refinement box (*i.e.*, the one containing the BH) to be sufficiently large so as to accommodate the AH as it grows. Clearly, this requirement becomes particularly important for

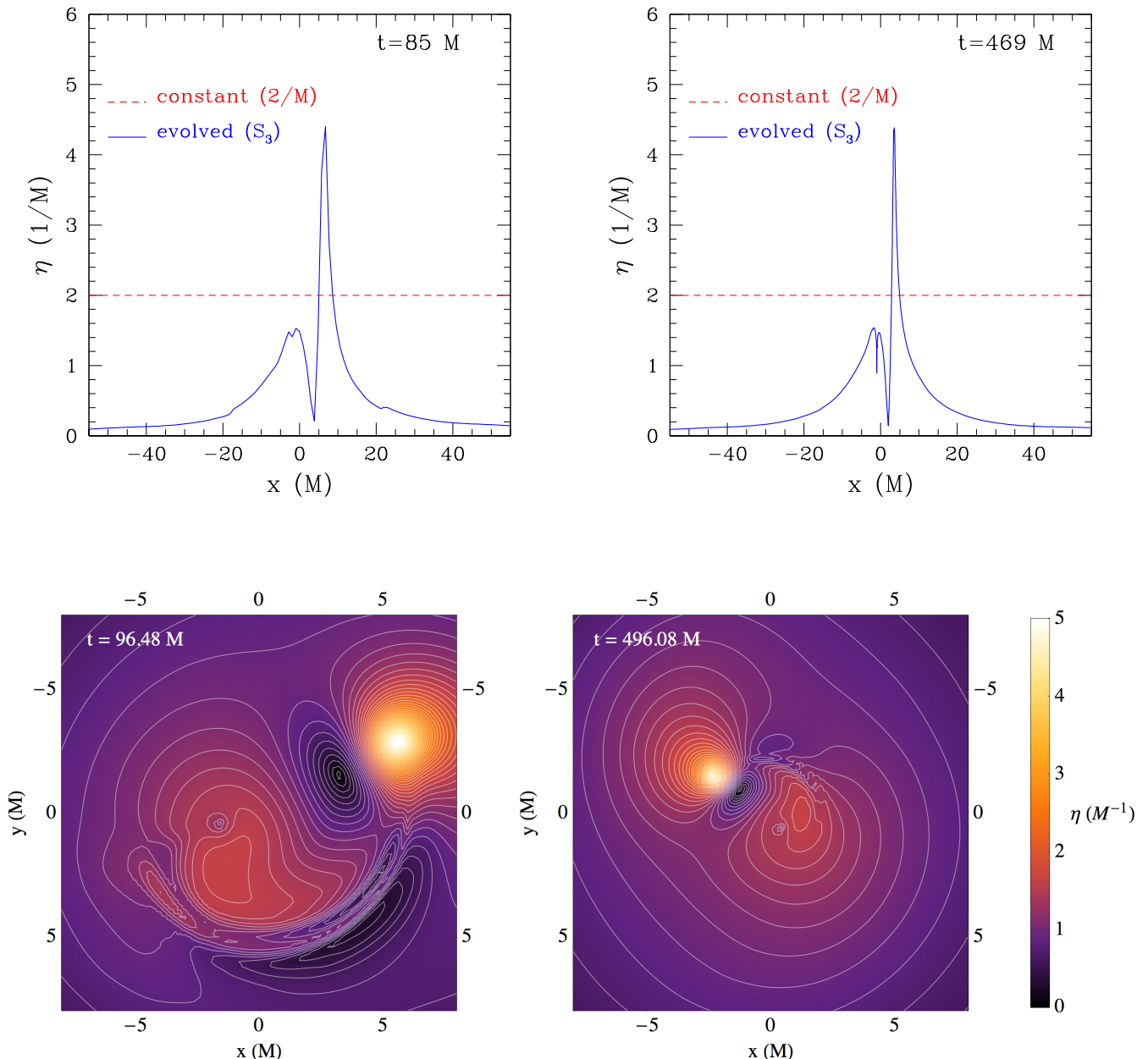


FIG. 5: Spatial dependence of the damping term  $\eta$  for an *unequal-mass* BBH system with  $q = 1/4$ . Different lines refer to the case when  $\eta$  is kept constant in space and time (red dashed line) or when it is evolved in time using Eq. (9) with source given by (14) (blue solid line). The top left and right panels refer to two different times when the punctures are close to the  $x$ -axis and show that the new gauge drives the damping term to follow the BHs and be smooth elsewhere. The bottom left and right panels, instead, show the damping term on the  $(x, y)$  plane at two representative times and show the non trivial but smooth distribution of the damping term which adapts to the motion of the punctures (the latter are near the maxima of the  $\eta$ ).

binaries with very small ratios, as in this case it is desirable to have the least dynamics and thus reduce the computational costs.

To report the ability of the new gauge to reduce the variations in the AH size, we show in the left panel of Fig. 8 the time evolution of the average radii of the unequal-mass binary on the  $(x, y)$  plane before and after the merger. We recall that during the inspiral and merger we follow three different AHs,

two corresponding to the initial BHs (*i.e.*,  $AH_1$  and  $AH_2$ ) and a third one, which is produced at the merger and contains the first two (*i.e.*,  $AH_3$ ). We also note that the two initial AHs can still be followed for a certain amount of time after a single AH is found comprising the two. Shown in the left panel of Fig. 8 with red long-dashed (large BH), dot-dashed (small BH) and dashed lines (merged BH) are the radii obtained for the case in which  $\eta$  is kept constant in space and time. The

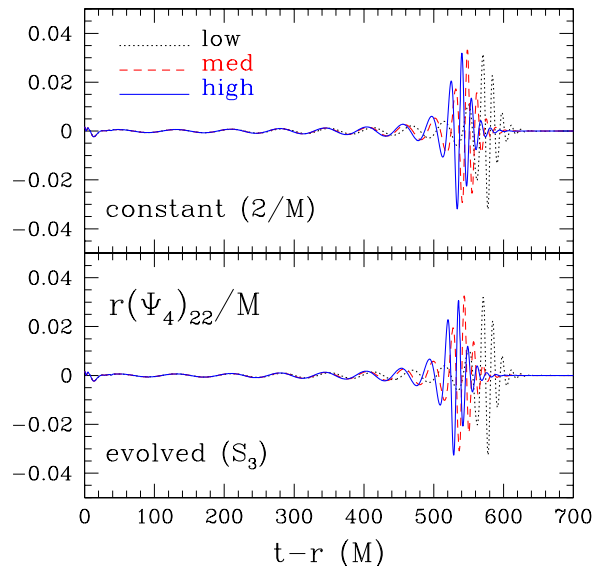


FIG. 6: Real part of the  $\ell = 2, m = 2$  mode of the gravitational waveform  $\Psi_4$  for the unequal-mass black-hole binary. Different lines refer to different resolutions (see text for details) and the two panels refer to the case when  $\eta$  is kept constant in space and time (upper panel) or when it is evolved with source given by (14) (lower panel).

radii obtained when  $\eta$  is evolved with source given by (14) are shown with blue solid (large BH), dotted (small BH) and short-dashed lines (merged BH).

In each case, the individual AHs first grow in radius as they initially adapt to the chosen gauge, *i.e.*, for  $t \lesssim 20 M$ . After this initial stage, however, the two gauges show a different behaviour and in the new gauge the AHs tend to maintain their coordinate size more closely than in the constant- $\eta$  case (*cf.* blue solid and red dashed lines). This ability to conserve the original size is evident also after the formation of the common AH at  $t \simeq 520 M$ , where the new gauge shows an average radius for  $AH_3$  which is essentially constant for  $t \sim 200 M$ , while it grows of about 10% over the same timescale when using a constant  $\eta$  gauge. These effects provide benefits for the mesh-refinement-treatment in our BBH simulations. Namely, they allow us to reduce the extent of the finest mesh-refinement levels containing the AHs and reduce therefore the computational cost of the simulations while keeping a given resolution.

Besides the changes in the overall coordinate size of the AHs discussed above, it is interesting to consider how much their shape changes in time in the two gauges and this is summarised in the right panel of Fig. 8, where we show the evolution of the ratio of the AHs’ proper circumferences on the  $(x, z)$  and  $(x, y)$  planes,  $\mathcal{C}_{xz}/\mathcal{C}_{yz}$ , as computed for the three BHs (the first two panels from the top refer to the AHs of the binary, while the third one to the merged AH and thus a different time range). Overall, in both gauges the merging BHs remain spherical to a few parts per thousand. We have also verified that the masses of the BHs as computed from the AHs are consistent between the two gauges within numeri-

cal errors. Interestingly, the new gauge leads to smaller oscillations in the ratio for the smallest of the BHs. This is a very small improvement, which however minimises spurious gauge-dynamics and helps when making AH-based measurements.

## VI. CONCLUSIONS

Even with a complete computational infrastructure, numerical-relativity simulations of inspiralling compact binaries would not be possible without suitable gauge conditions. A large bulk of work developed over the last decade has provided gauge conditions for the lapse and the shift which have been used with success both in vacuum and non-vacuum spacetimes when simulating binaries with comparable masses. However, as the need to investigate black-hole binaries with small mass ratios increases, evidence has emerged that the standard “Gamma-driver” shift condition requires a careful and non-trivial tuning of its parameters to ensure long-term stable evolutions of such binaries.

As a result, a few different suggestions have been made recently in the literature to improve the Gamma-driver condition for the shift and these have focused, in particular, on the specification of a spatially dependent damping term  $\eta$ . This approach has been shown to work well under some conditions but not always and prescriptions which are effective in some cases can lead to instabilities in others. In addition, the prescriptions require the specification of coefficients whose tuning may be dependent on the mass ratio in a way which is not trivial.

Following a different approach, we have presented a novel gauge condition in which the damping constant is promoted to be a dynamical variable and the solution of an evolution equation. We show that this choice removes the need for special tuning and provides a shift damping term which is free of instabilities for all of the spacetimes considered. Although rather trivial, our gauge condition has a number of advantages: *i)* it is very simple to implement numerically as it has the same structure of the other gauge conditions; *ii)* it adapts dynamically to the individual positions and masses of the BBH system and could therefore be used also for binaries with very small mass ratios; *iii)* it reduces the variations in the coordinate size of the apparent horizon of the larger black hole thus limiting the computational costs; *iv)* all of the complexity in the new gauge is contained in the source function which can be easily improved further. This last point will be part of our future research in this direction.

## Acknowledgments

It is a pleasure to thank Jose-Luis Jaramillo for useful discussions. This work was supported in part by the DFG grant SFB/Transregio 7 “Gravitational-Wave Astronomy”. The computations were performed on the Damiana cluster at the AEI, at LRZ Munich, on the LONI network

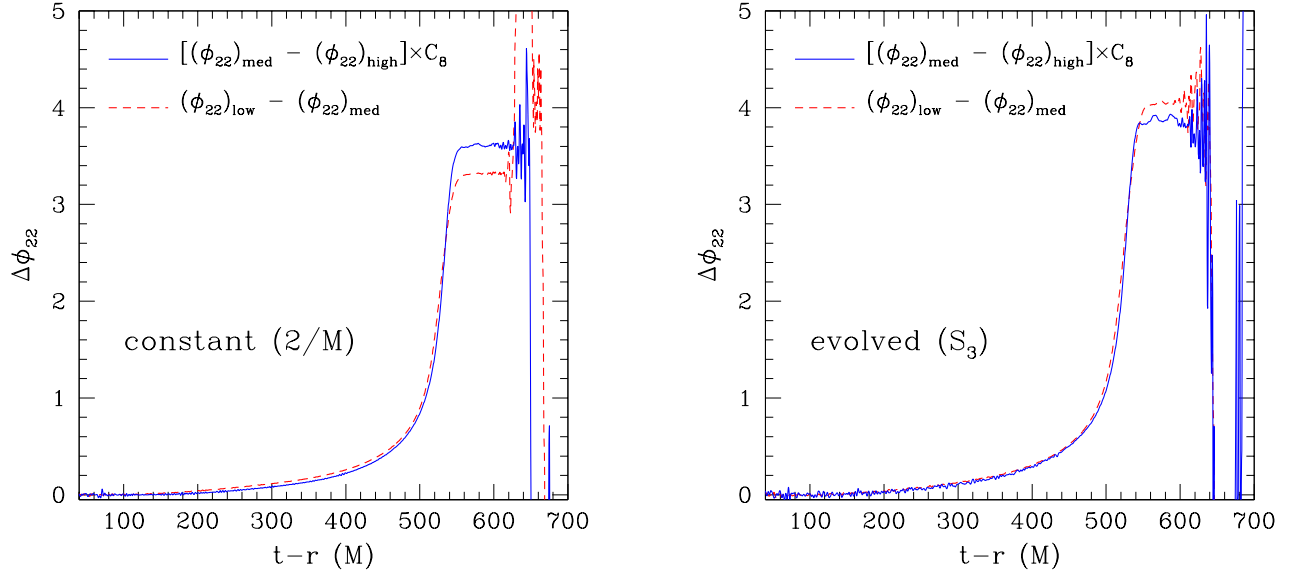


FIG. 7: Phase difference in the  $\ell = 2, m = 2$  mode of the gravitational waveforms as computed between the low and medium resolutions (red dashed line) and between the medium and high resolutions (blue solid line). The latter has been scaled to compensate for an 8th-order convergence which is indeed obtained as shown by the good overlap between the curves. The left panel refers to the case when  $\eta$  is kept constant in space and time, while the right one to when it is evolved with source given by (14).

([www.loni.org](http://www.loni.org)), and on the Teragrid network (allocation TG-MCA02N014).

- 
- [1] F. Pretorius, *Phys. Rev. Lett.* **95**, 121101 (2005).  
[2] M. Campanelli, C. O. Lousto, P. Marronetti, and Y. Zlochower, *Phys. Rev. Lett.* **96**, 111101 (2006).  
[3] J. G. Baker, J. Centrella, D.-I. Choi, M. Koppitz, and J. van Meter, *Phys. Rev. Lett.* **96**, 111102 (2006).  
[4] I. Hinder, *Class. Quant. Grav.* **27**, 114004 (2010).  
[5] M. Campanelli et al., *Class. Quant. Grav.* **27**, 084034 (2010).  
[6] P. Ajith et al., *Class. Quant. Grav.* **24**, S689 (2007).  
[7] P. Ajith et al., *Phys. Re. D* **77**, 104017 (2008).  
[8] P. Ajith, *Class. Quant. Grav.* **25**, 114033 (2008).  
[9] B. Aylott et al., *Class. Quant. Grav.* **26**, 165008 (2009).  
[10] B. Farr, S. Fairhurst, and B. S. Sathyaprakash, *Class. Quant. Grav.* **26**, 114009 (2009).  
[11] L. Santamaria, B. Krishnan, and J. T. Whelan, *Class. Quant. Grav.* **26**, 114010 (2009).  
[12] L. Rezzolla, *Class. Quant. Grav.* **26**, 094023 (2009).  
[13] E. Barausse and L. Rezzolla, *Astrophys. J. Lett.* **704**, L40 (2009).  
[14] J. R. van Meter, M. C. Miller, J. G. Baker, W. D. Boggs, and B. J. Kelly, [arXiv:1003.3865](https://arxiv.org/abs/1003.3865) (2010).  
[15] E. Berti and M. Volonteri, *Astrophys. J.* **684**, 822 (2008).  
[16] N. Fanidakis, C. M. Baugh, S. Cole, and C. S. Frenk, *Journal of Physics Conference Series* **189**, 012013 (2009).  
[17] C. Palenzuela, L. Lehner, and S. Yoshida, *Phys. Rev. D* **81**, 084007 (2010).  
[18] P. Mösta, C. Palenzuela, L. Rezzolla, L. Lehner, S. Yoshida, and D. Pollney, *Phys. Rev. D* **81**, 064017 (2010).  
[19] T. Bode, R. Haas, T. Bogdanovic, P. Laguna, and D. Shoemaker, *Astrophys. J.* **715**, 1117 (2010).  
[20] B. D. Farris, Y. T. Liu, and S. L. Shapiro, *Phys. Rev. D* **81**, 084008 (2010).  
[21] S. Dain, C. O. Lousto, and Y. Zlochower, *Physical Review D* **78**, 024039 (2008).  
[22] J. A. Gonzalez, U. Sperhake, and B. Brügmann, *Phys. Rev. D* **79**, 124006 (2009).  
[23] C. O. Lousto, H. Nakano, Y. Zlochower, and M. Campanelli, *Phys. Rev. Lett.* **104**, 211101 (2010).  
[24] M. Alcubierre, B. Brügmann, P. Diener, M. Koppitz, D. Pollney, E. Seidel, and R. Takahashi, *Phys. Rev. D* **67**, 084023 (2003).  
[25] D. Müller and B. Brügmann, *Class. Quant. Grav.* **27**, 114008 (2010).  
[26] D. Müller, J. Grigsby, and B. Brügmann, *Phys. Rev.* **D82**, 064004 (2010).  
[27] E. Schnetter, *Class. Quant. Grav.* **27**, 167001 (2010).  
[28] D. Pollney, C. Reisswig, L. Rezzolla, B. Szilágyi, M. Ansorg, B. Deris, P. Diener, E. N. Dorband, M. Koppitz, A. Nagar, et al., *Phys. Rev. D* **76**, 124002 (2007).  
[29] D. Pollney, C. Reisswig, E. Schnetter, N. Dorband, and P. Diener, [arXiv:0910.3803](https://arxiv.org/abs/0910.3803) (2009).  
[30] T. Goodale, G. Allen, G. Lanfermann, J. Massó, T. Radke, E. Seidel, and J. Shalf, in *Vector and Parallel Processing – VECPAR’2002, 5th International Conference, Lecture Notes in Computer Science* (Springer, Berlin, 2003).  
[31] <http://www.cactuscode.org>.  
[32] E. Schnetter, S. H. Hawley, and I. Hawke, *Class. Quantum Grav.* **21**, 1465 (2004).  
[33] Mesh Refinement with Carpet, URL <http://www.carpetcode.org/>.  
[34] C. Bona, J. Massó, E. Seidel, and J. Stela, *Phys. Rev. Lett.* **75**, 600 (1995).

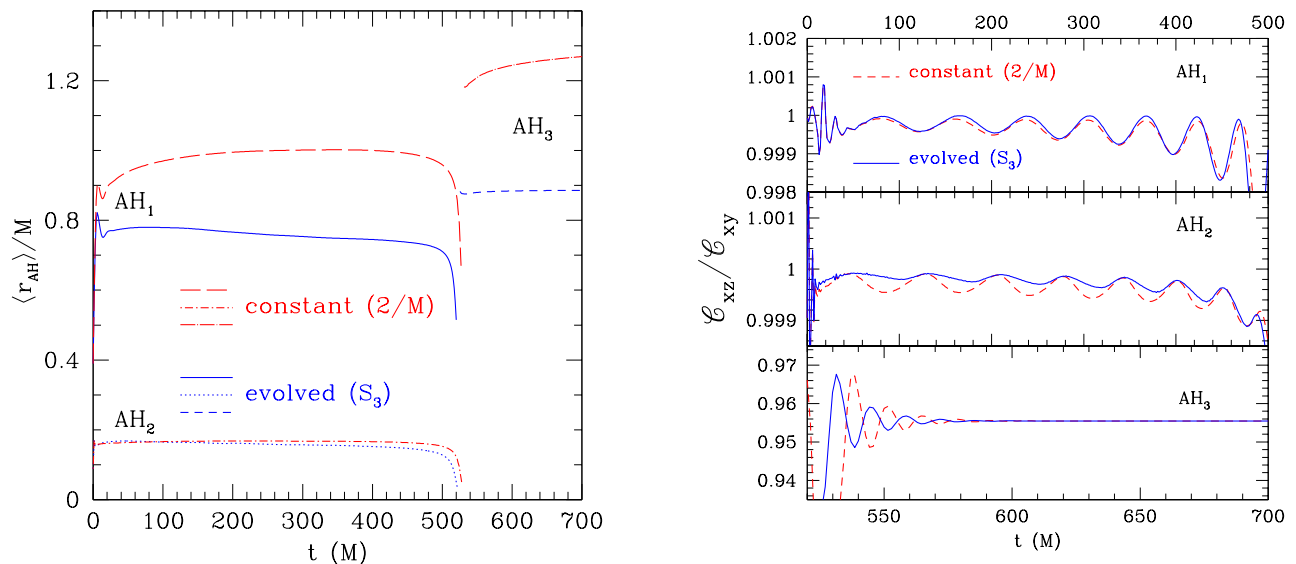


FIG. 8: *Left panel:* Evolution of the average radius of the AHs on the  $(x, y)$  plane before and after the merger. Shown with red long-dashed (large BH), dot-dashed (small BH) and dashed lines (merged BH) are the radii obtained for the case in which  $\eta$  is kept constant in space and time. Shown instead with blue solid (large BH), dotted (small BH) and short-dashed lines (merged BH) are the radii obtained for the case in which  $\eta$  is evolved with source given by (14). *Right panel:* Evolution of the ratio of the AHs' proper circumferences on the  $(x, z)$  and  $(x, y)$  planes,  $\mathcal{C}_{xz}, \mathcal{C}_{xy}$ , as computed for the three BHs. The first two panels from the top refer to the AHs of the binary, while the bottom one refers to the merged AH and thus covers a different range in time.

[35] L. Smarr and J. W. York, Phys. Rev. D **17**, 2529 (1978).

[36] L. Baiotti, I. Hawke, P. J. Montero, F. Löffler, L. Rezzolla, N. Stergioulas, J. A. Font, and E. Seidel, Phys. Rev. D **71**, 024035 (2005).

[37] M. Alcubierre, A. Corichi, J. A. González, D. Núñez, and M. Salgado, Class. Quantum Grav. **20**, 3951 (2003).

[38] L. Baiotti, B. Giacomazzo, and L. Rezzolla, Phys. Rev. D **78**, 084033 (2008).

[39] L. Rezzolla, L. Baiotti, B. Giacomazzo, D. Link, and J.-A. Font, Class. Quantum Grav. **27**, 114105 (2010).

[40] F. Löffler, L. Rezzolla, and M. Ansorg, Phys. Rev. D **74**, 104018 (2006).

[41] M. Hannam, S. Husa, F. Ohme, B. Brügmann, and N. Ó Murchadha, Phys. Rev. D **78**, 064020 (2008).